ARTICLE

Hydrated Lithium *nido*-Boranes for Solid-Liquid Hybrid Batteries†

Diego H. P. Souza,[a] Terry D. Humphries,[a] Yu Liu,[a] Anton Gradišek,[b] Anita M. D'Angelo,[c] Craig E. Buckley,[a] and Mark Paskevicius[a]*

Received 00th January 20xx,
Accepted 00th January 20xx

DOI: 10.1039/x0xx00000x

Hydridoborate salts are considered as promising solid-state electrolyte candidates for the development of solid-state batteries (SSBs). The presence of coordinated water in the crystal structure may facilitate the migration of the cation, yielding compounds with high ionic conductivity. In the present study, two samples of hydrated $LiB_{11}H_{14}$, here called $LiB_{11}H_{14}{\cdot}2H_2O$ and *a*-$LiB_{11}H_{14}{\cdot}(H_2O)_n$ (n < 2), demonstrate remarkably different properties as solid-state electrolytes. $LiB_{11}H_{14}{\cdot}2H_2O$ is identified as a new class of ionic liquid, as it melts at ≈ 70 °C, whereas the sample *a*-$LiB_{11}H_{14}{\cdot}(H_2O)_n$ undergoes a polymorphic phase transition close to this temperature, reaching the liquid-like ionic conductivity of 3.2 x 10^{-2} S cm^{-1} at 70 °C and an oxidative stability limit of 2.8 V against Li^+/Li. Galvanostatic cycling and battery tests were conducted with *a*-$LiB_{11}H_{14}{\cdot}(H_2O)_n$ as the solid-state electrolyte (SSE) at 60°C with the addition of traces of either the ionic liquid (IL) $LiB_{11}H_{14}{\cdot}2H_2O$ or the liquid electrolyte (LE) 1.0 M $LiPF_6$ EC/DMC (*v/v* = 50/50) at their interfaces. Galvanostatic experiments for the cell Li/IL/SSE/IL/Li showed an overpotential of only 21 mV after 9 days cycling (48 h at 25 µA cm^{-2} and 168 h at 50 µA cm^{-2}), and the battery Li/LE/SSE/SSE+TiS_2 retained 83% of its capacity shown in the first cycle at 0.4 *C* after 50 cycles. $LiB_{11}H_{14}{\cdot}2H_2O$ and 1.0 M $LiPF_6$ EC/DMC work effectively as wetting agents to improve SSE/Li contact.

Introduction

Liquid-based lithium-ion batteries (LIBs) have been used to power the majority of electronic devices for the last three decades due to their long cycle life and ability to quickly charge.[1,2] However, the development of high-power technologies, such as electric vehicles and large-scale energy storage, require batteries with higher energy density, durability, lower costs and lighter components.[3] Those limitations have brought extensive research on the development of solid-state electrolytes to replace the liquid component of the current generation LIBs as an attempt to resolve their drawbacks.[4,5] Solid-state electrolytes can provide higher thermal stability, improved safety and higher energy storage capacity, as they can be compatible with alternative electrode materials, e.g. lithium metal, which is the target anode material due to its low redox potential (-3.04 V *vs*. standard hydrogen electrode) and high theoretical capacity (3,860 mAh g^{-1}).[6–9]

In order to develop the next generation of batteries, the solid-state electrolyte must meet several requirements, including, but not limited to, high ionic conductivity (≥ 1 x 10^{-3} S cm^{-1}), wide electrochemical stability, compatibility with anode and cathode materials, affordable cost, be an electrical insulator and environmentally friendly.[1,10,11] The interfacial resistance between a solid-state electrolyte and the electrode (SSE/electrode) is also a crucial factor for practical solid-state battery applications.[12,13] The formation of a solid-liquid hybrid electrolyte is now seen as a strategy to overcome this issue.[14,15] It has been proven that wetting the interface with the addition of a small amount of an ionic liquid[16–18] or an organic liquid electrolyte[19–21] can improve interfacial contact and performance of the battery.[13]

Oxides[22,23] and sulphides[24,25] are commonly studied materials as solid-state electrolytes due to their high ionic conductivities, however some aspects, such as, low electrochemical stability, high interfacial resistance and/or high costs for large-scale production hinder their use in solid-state batteries (SSBs).[26,27] Lithium boron-hydrogen salts have been recently investigated as solid-state electrolytes due to the disordered polymorphic crystal structures with high ionic conductivity that some of them can assume at higher than ambient temperatures.[28–34] Moreover, some of them present stability against the lithium metal anode[11,35] and a reproducible manufacturing processes.[11] Several attempts to stabilise the superionically conductive high temperature polymorphs to room temperature or to increase the room temperature Li^+ conductivity of the boron-hydrogen salts have already been conducted with some successful strategies, such as chemical and/or mechanical modification.[32,35–40] The coordination of the borane salts with small neutral molecules, such as water and ammonia, also seem to increase their ionic conductivity as those molecules may facilitate the migration of the cation through the crystal structure.[41–43]

Recently, the hydrated *nido*-borane lithium tetradecahydroundecaborane ($LiB_{11}H_{14}{\cdot}(H_2O)_n$), with cubic

[a] *Department of Physics and Astronomy, Curtin University, GPO Box U1987, Perth, WA 6845, Australia.*
[b] *Jožef Stefan Institute, SI-1000 Ljubljana, Slovenia.*
[c] *Australian Synchrotron (ANSTO), Clayton, VIC 3168, Australia.*

†Electronic Supplementary Information (ESI) available: Experimental details. Raman, solution-state and solid-state NMR, XRPD, DSC/TGA, TPPA, and LSV data. Rietveld refinements, Nyquist and ionic conductivity plots, CCD and battery tests. *In-situ* XRPD and Temperature dependence of ^{11}B spin-lattice relaxation rates for *b*-$LiB_{11}H_{14}{\cdot}(H_2O)_n$. Supplementary tables. See DOI: 10.1039/x0xx00000x

space-group $Fm\bar{3}m$ at room temperature (RT), had its synthesis elucidated and ionic conductivity properties investigated.[42] This material exhibits a Li^+ conductivity of 1.8 x 10^{-4} S cm^{-1} at 25 °C, which is some of the highest Li^+ conductivities at RT among the boron-hydrogen salts.[42] Another recent study detailed the synthesis of dehydrated $LiB_{11}H_{14}$, which presents an orthorhombic unit cell with space group *Pbca* and ionic conductivity of 1.5 x 10^{-6} S cm^{-1} at RT. This sample undergoes a polymorphic phase transition at ≈ 112 °C assuming a disordered cubic $Fm\bar{3}$ space group and has a liquid-like ionic conductivity.[32] Some of the most promising lithium-boranes as solid-state electrolytes have carboranes in their structure, such as $0.7Li(CB_9H_{10})$-$0.3Li(CB_{11}H_{12})$ and $Li_3(B_{11}H_{14})(CB_9H_{10})_2$, which present ionic conductivities higher than 1 x 10^{-3} S cm^{-1} at 25 °C.[32,35] However, carboranes usually present high-costs due to the need for expensive and dangerous reagents, as well as, long synthetic processes.[44,45] The optimisation of synthetic processes of metal-boranes with reduced costs is important for further research and application as solid-state electrolyte.

Here, the synthesis of $LiB_{11}H_{14}$ with different levels of water content and structures are demonstrated through a facile method using common laboratory reagents, as well as, their thermal and solid-state electrochemical properties. Battery tests with the salt, here denoted as *a*-$LiB_{11}H_{14}\cdot(H_2O)_n$, were also performed using Li as the anode and TiS_2 as the cathode. A liquid electrolyte and an ionic liquid are used to investigate the effect of the interfacial contact over the performance of the battery. The difficulties that surround the application of *a*-$LiB_{11}H_{14}\cdot(H_2O)_n$ as solid-state electrolyte are also discussed in this paper for further consideration in solid-state electrolyte research.

Experimental

Chemicals

Sodium borohydride ($NaBH_4$, anhydrous, 98%), diglyme ($C_6H_{14}O_3$, anhydrous, 99.5%), 1-bromopentane ($C_5H_{11}Br$, 98%), diethyl ether ($(C_2H_5)_2O$, anhydrous, 99.7%), trimethylamine hydrochloride ($(CH_3)_3N\cdot HCl$, 98%), deuterated water (D_2O, 99.9 atom % D), deuterated acetonitrile (CD_3CN, 99.8 atom % D), lithium (Li ribbon, thickness 0.38 mm, 99.9%), graphite powder (< 20 µm), lithium hexafluorophosphate solution in ethylene carbonate and dimethyl carbonate (1.0 M $LiPF_6$ EC/DMC (*v/v* = 50/50)), titanium(IV) sulphide (TiS_2, 99.9%), acetonitrile (CH_3CN, anhydrous, 99.8%), boric acid (H_3BO_3, 99.5%) and platinum foil (Pt, 99.95%, thickness 0.1 mm) were all purchased from Sigma-Aldrich. Lithium hydroxide (LiOH, anhydrous, 98%) and gold foil (Au, 99.95%, thickness 0.1 mm) were obtained from Alfa Aesar, acetone (C_3H_6O, 99.5%) from Unilab, and hydrochloric acid (HCl, 37%) from Scharlau. In order to maintain an inert atmosphere, all chemicals and samples were manipulated in an argon filled glovebox (Mbraun, O_2 & H_2O < 1 ppm) or using Schlenk techniques under argon.

Characterisation

Raman spectroscopy, solution-state and solid-state Nuclear Magnetic Resonance Spectroscopy (NMR), X-ray Powder Diffraction (XRPD), simultaneous Thermogravimetry (TGA) and Differential Scanning Calorimetry analysis (DSC), Temperature Programmed Photographic Analysis (TPPA) and Electrochemical Impedance Spectroscopy (EIS) were used to characterise the samples. The samples *a*-$LiB_{11}H_{14}\cdot(H_2O)_n$ and *b*-$LiB_{11}H_{14}\cdot(H_2O)_n$ were also characterised through *in situ* Synchrotron Radiation X-Ray Powder Diffraction (SR-XRPD) upon cooling and heating, respectively. *b*-$LiB_{11}H_{14}\cdot(H_2O)_n$ also had its ^{11}B spin-lattice NMR relaxation rates analysed vs temperature. Battery tests and electrochemical measurements, such as Linear Sweep Voltammetry (LSV), Galvanostatic Cycling (GC) and Critical Current Density (CCD) were performed with the sample *a*-$LiB_{11}H_{14}\cdot(H_2O)_n$ as the solid-state electrolyte. Some measurements were conducted with the addition of $LiB_{11}H_{14}\cdot 2H_2O$ on the interface of the SSE and cathode/anode, and other measurements with the addition of one drop of 1.0 M $LiPF_6$ EC/DMC for comparison of results. Detailed information for all analyses can be found in the Electronic Supplementary Information.

Synthesis of lithium *nido*-tetradecahydroundecaborane, $LiB_{11}H_{14}\cdot 2H_2O$, *a*-$LiB_{11}H_{14}\cdot(H_2O)_n$ (n < 2), and $LiB_{11}H_{14}$

$LiB_{11}H_{14}\cdot 2H_2O$ was prepared based on the reaction of $(CH_3)_3NHB_{11}H_{14}$ and LiOH in aqueous solution according to reaction 1, containing 40% excess LiOH:

$$(CH_3)_3NHB_{11}H_{14(aq)} + LiOH_{(aq)} \xrightarrow{H_2O,\ 100\ °C} LiB_{11}H_{14(aq)} + (CH_3)_3N_{(g)} + H_2O_{(l)} \quad (1)$$

$(CH_3)_3NHB_{11}H_{14}$ was synthesised according to a previously reported method.[42] This material was further recrystallised by dissolution in a hot aqueous solution of acetone (10% acetone).[44] The colourless precipitate was collected by filtration, washed with cold Milli-Q water and dried in *vacuo* at 90 °C. 140 mg of lithium hydroxide (5.85 mmol) was dissolved in 40 mL of Milli-Q water (0.15 mol L^{-1}), and 800 mg of recrystallised $(CH_3)_3NHB_{11}H_{14}$ (4.14 mmol) was added to this solution. To ensure dissolution of the powder, the mixture was sonicated several times and stirred at room temperature. The aqueous solution was stirred at 100 °C for ≈ 15 minutes in an open vessel to ensure elimination of trimethylammonium cation, $(CH_3)_3NH^+$, as trimethylamine gas, $(CH_3)_3N$. After cooling to room temperature, the suspension formed was filtered, and the filtrate dried at 80 °C under vacuum for 2 hours. No additional step for removal of excess LiOH or possible byproducts was taken. This yielded 0.60 g (3.41 mmol, 82% yield) of a deliquescent colourless powder of $LiB_{11}H_{14}\cdot 2H_2O$.

In order to synthesise $LiB_{11}H_{14}\cdot(H_2O)_n$ with n < 2, the same methodology to prepare $LiB_{11}H_{14}\cdot 2H_2O$ was used, however different heating times to dry the sample were applied. For *a*-$LiB_{11}H_{14}\cdot(H_2O)_n$, the filtrate was dried for 4 hours in *vacuo* at 80 °C, yielding 0.52 g of the material. For anhydrous $LiB_{11}H_{14}$, the filtrate was dried for 20 hours *in vacuo* at 110 °C, yielding 0.46 g of sample (3.29 mmol, 79% yield).

Synthesis of hydrated lithium *nido*-tetradecahydroundecaborane ($Fm\bar{3}m$ polymorph), *b*-$LiB_{11}H_{14}\cdot(H_2O)_n$

The synthesis of *b*-$LiB_{11}H_{14}\cdot(H_2O)_n$ was performed by following the same methodology previously reported.[42] 600 mg of $(CH_3)_3NHB_{11}H_{14}$ was dissolved into 40 mL of an aqueous solution of LiOH (0.47 mol L^{-1}), which was heated at 100 °C for 15 minutes in an open vessel. At room temperature, the solution was filtered, the filtrate was reheated to 90 °C and had its pH adjusted to ≈ 4.5 using an aqueous solution of HCl 2%. The solution was then washed with diethyl ether at room temperature, and the organic layer was flushed with argon and dried *in vacuo* at 80 °C to crystallise the known cubic $Fm\bar{3}m$ polymorph.

Results and discussion

Sample characterisation

The samples were characterised through Raman spectroscopy (Fig. S1), and the presence of B–H bonds was confirmed by Raman modes at around 2500 cm^{-1}.[47–49] The lack of a N–H Raman shift between 3400 - 3200 cm^{-1} that would be observed from unreacted $(CH_3)_3NHB_{11}H_{14}$ was not detected, confirming that there is no remnant trimethylammonium-borane in the solid.[42,50] Moreover, the presence of water was confirmed for samples $LiB_{11}H_{14}\cdot2H_2O$ and *a*-$LiB_{11}H_{14}\cdot(H_2O)_n$ through the observation of an O–H stretching band at 3600 – 3450 cm^{-1}.[51] The intensity of this band is higher in the doubly hydrated salt than in *a*-$LiB_{11}H_{14}\cdot(H_2O)_n$, as the latter contains less water molecules. The same O–H mode was not observed for $LiB_{11}H_{14}$, which suggests that the heating treatment that was applied to dry this sample was enough to obtain an anhydrous salt. The Raman mode observed at ≈ 770 cm^{-1} in all samples may be related to the presence of B–O bonds from an amorphous borate byproduct, e. g. $LiB(OH)_4$, that is formed and remains in the composition of the solid.[52–54]

^{11}B NMR spectroscopy (Fig. S2) was conducted in deuterated acetonitrile (CD_3CN), and $B_{11}H_{14}^-$ resonances (δ = −14.2, −16.0 and −16.8 ppm) were identified in the spectra of all samples.[32,42] The presence of additional resonances representing $B_{11}H_{13}OH^-$ at δ = 18.8, −9.6, −10.7, −23.3, −29.1, and −40.0 ppm can only be observed in the spectrum of anhydrous $LiB_{11}H_{14}$.[42] The formation of this species is expected for samples of $B_{11}H_{14}^-$ and other boron-hydrogen salts, such as $B_{12}H_{12}^{2-}$ and $B_{10}H_{10}^{2-}$, when exposed to long periods of heating and/or dehydration.[42,55]

It is important to highlight that a white precipitate was formed in the NMR tube for all samples after dissolution of the salts in acetonitrile. In order to further investigate the composition of that precipitate, 40 mg of *a*-$LiB_{11}H_{14}\cdot(H_2O)_n$ was mixed with 6 mL of acetonitrile and sonicated several times at room temperature, which formed a white precipitate. After filtration, an aliquot of the filtrate was dissolved into CD_3CN, and an aliquot of the residue was dissolved into D_2O for further NMR analysis. Fig. S3 shows that the filtrate contained $B_{11}H_{14}^-$, whereas the NMR spectrum of the residue shows the presence of a borate species. Solid-state ^{11}B NMR spectroscopy of *a*-$LiB_{11}H_{14}\cdot(H_2O)_n$ (Fig. S4) also reveals the presence of $B_{11}H_{14}^-$, which was compared with the spectrum of the previously reported $LiB_{11}H_{14}\cdot(H_2O)_n$ in the $Fm\bar{3}m$ space-group (denoted here as *b*-$LiB_{11}H_{14}\cdot(H_2O)_n$),[42] and a borate species at a chemical shift of ≈ 1 ppm. Boric acid is formed as a byproduct of the reaction of $(CH_3)_3NHB_{11}H_{14}$ with an alkaline metal hydroxide in aqueous solution.[42] The reaction of unreacted lithium hydroxide with boric acid forms a lithium borate species, e.g. $LiB(OH)_4$, that is observed through solid-state ^{11}B NMR spectroscopy at ≈ 1 ppm (Fig. S4).[56,57] In aqueous solution, an equilibrium exists between $B(OH)_4^-$ and H_3BO_3, according to equation 2, which shifts the ^{11}B NMR chemical signal of the borate species as a function of pH in the range of 1 - 20 ppm (Fig. S3).[58]

$$B(OH)_{4(s)}^- \rightleftarrows OH_{(aq)}^- + H_3BO_{3(aq)} \quad (2)$$

XRPD patterns of $LiB_{11}H_{14}\cdot2H_2O$, *a*-$LiB_{11}H_{14}\cdot(H_2O)_n$, and $LiB_{11}H_{14}$ are illustrated in Fig. 1. The presence of unreacted LiOH or any crystalline borate species were not observed in any diffraction pattern, which suggests the presence of an amorphous borate compound, in conjunction with ^{11}B NMR and Raman spectroscopy results.

The formation of lithium borate species from the reaction of lithium hydroxide and boric acid in aqueous solution has been previously reported.[59] Furthermore, as a test, 0.1 g of H_3BO_3 was dissolved into 30 mL of an aqueous solution containing 0.1 g of LiOH, and that solution was submitted to the same process that is conducted to synthesise any $LiB_{11}H_{14}$ reported here. Therefore, the solution was heated at 100 °C for 15 minutes in

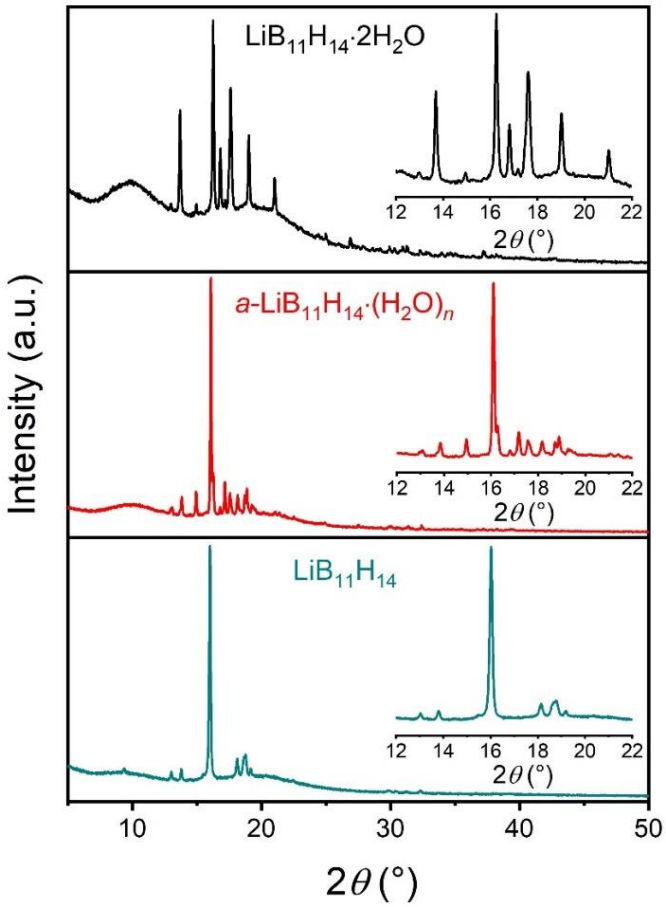

Fig. 1. XRPD pattern for $LiB_{11}H_{14}\cdot2H_2O$, *a*-$LiB_{11}H_{14}\cdot(H_2O)_n$, and $LiB_{11}H_{14}$ at room temperature with magnified insets in the range of 2Θ = 12 – 22°. λ = 1.54056 Å.

an open vessel, filtered at room temperature and left drying in *vacuo* at 80 °C. The resulting white solid was characterised through XRPD and ^{11}B NMR in D_2O at room temperature (Fig. S5). The XRPD pattern infers the formation of an amorphous $LiB(OH)_4$ structure, and solution-state ^{11}B NMR shows a peak at 1.6 ppm, which is in agreement with the chemical shift of $B(OH)_4^-$ in a high pH aqueous solution.[58] These results suggest that all samples of $LiB_{11}H_{14}$ presented here do not contain any unreacted LiOH, but instead contain some quantity of an amorphous lithium borate species.

Rietveld refinement analysis of $LiB_{11}H_{14}{\cdot}2H_2O$ XRPD data (Fig. S6) reveals that the material is predominantly formed by the dihydrate in the monoclinic space group *C*2/*c* (97.0(3) wt%), which is the same as that previously reported from single-crystal XRPD data.[42] The presence of a minor amount (3.0(3) wt%) of a compound in the orthorhombic space-group *Pbcn* (*a* = 41.431(30) Å, *b* = 10.114(8) Å, *c* = 10.454(11) Å, *V*/*Z* = 273.8 Å^3) can also be observed in the diffractogram of this sample (indexing details below, also see Table S1). DSC-TGA was conducted on $LiB_{11}H_{14}{\cdot}2H_2O$ in order to investigate its thermal behaviour (Fig. S7). A strong endothermic event was observed at 73 °C, which was first assumed to be related to a polymorphic phase transition. However, TPPA (Fig. S8) shows that the pellet of $LiB_{11}H_{14}{\cdot}2H_2O$ becomes a liquid at ≈ 70 °C, therefore, the endothermic peak corresponds to the melting point of the material. The DSC-TGA plot also showed an exothermic peak at 230 °C with a corresponding weight loss of 12.5(2)%, indicative of its decomposition (Fig. S7). TPPA also showed that the sample becomes a solid again above 200 °C, along with water loss and the subsequent change to a yellow colour. It should be noted that salts with low melting points below 100 °C, are classified as ionic liquids, of which most are composed of an organic cation and an inorganic anion.[60,61] Furthermore, ionic liquids present several different applications, including chemical reactions as solvents or catalysts and in energy storage applications as electrolyte materials.[60–63] $LiB_{11}H_{14}{\cdot}2H_2O$ is reported here as a new class of ionic liquid, which is simple to prepare, free of an organic component and should therefore be further studied for future battery applications. It is important to clarify that the water in this system is not 'free water', instead it is strongly bound to the Li^+ cation in the salt as a solvated molecule.[42] Thus the ionic liquid, or molten $LiB_{11}H_{14}.2H_2O$, is simply a molten salt, not a wet salt. This means that the H_2O molecules are bound to the Li^+ cation and are less prone to reacting with other parts of a battery due to enhanced electrochemical stability.[64,65]

To understand its thermal behaviour, *a*-$LiB_{11}H_{14}{\cdot}(H_2O)_n$ was analysed through SR-XRPD, and the RT and HT (high temperature, 100 °C) data were treated by Rietveld refinement (Fig. S9). The sample measured at RT is a mixture of three $LiB_{11}H_{14}$ containing compounds. Two of the major phases were $LiB_{11}H_{14}$ (space group *Pbca*, 70.0(1) wt%)[32] and $LiB_{11}H_{14}{\cdot}2H_2O$ (space group *C*2/*c*, 4.10(11) wt%)[42] (Table S1). The second most abundant phase was indexed in the orthorhombic space group *Pbcn* with lattice parameters *a* = 41.446(1) Å, *b* = 10.127(1) Å, *c* = 10.440(1) Å, and *V*/*Z* = 273.9 Å^3. As this phase was only present as 25.9(1) wt% of the sample, it was not possible to solve the structure, although it is deemed that it is a hydrated $LiB_{11}H_{14}$ complex. As such, the sample itself is denoted as *a*-$LiB_{11}H_{14}{\cdot}(H_2O)_n$ with an unknown water content. Upon heating past 70 °C, this mixture of $LiB_{11}H_{14}$ and its hydrates undergoes a polymorphic phase transition to a cubic HT polymorph (Fig. 2 and S9).

It has been reported that dehydrated $LiB_{11}H_{14}$ undergoes an orthorhombic to cubic polymorphic phase change at ≈ 110 °C.[32] Therefore, it is proposed that the presence of hydrates reduces the cubic polymorphic phase transition temperature closer to RT. The structure observed for the HT *a*-$LiB_{11}H_{14}{\cdot}(H_2O)_n$ at 100 °C was indexed in cubic space group $Ia\bar{3}d$ with *a* = 14.399(1) Å and *V* = 2985.6(1) Å^3 (Table S1 and Fig. S9). Anhydrous $LiB_{11}H_{14}$ was previously indexed in space group $Fm\bar{3}$ (*a* = 9.9465(6) Å) at high temperature (140 °C).[32] Unfortunately, due to the inherently disordered structure and possible dynamics of the $B_{11}H_{14}^-$ anions along with the fractional coordinated water, it was not possible to solve the crystal structure for HT *a*-$LiB_{11}H_{14}{\cdot}(H_2O)_n$.

DSC/TGA data for *a*-$LiB_{11}H_{14}{\cdot}(H_2O)_n$ (Fig. S10) demonstrated an endothermic event at ≈ 70 °C, which corresponds to the

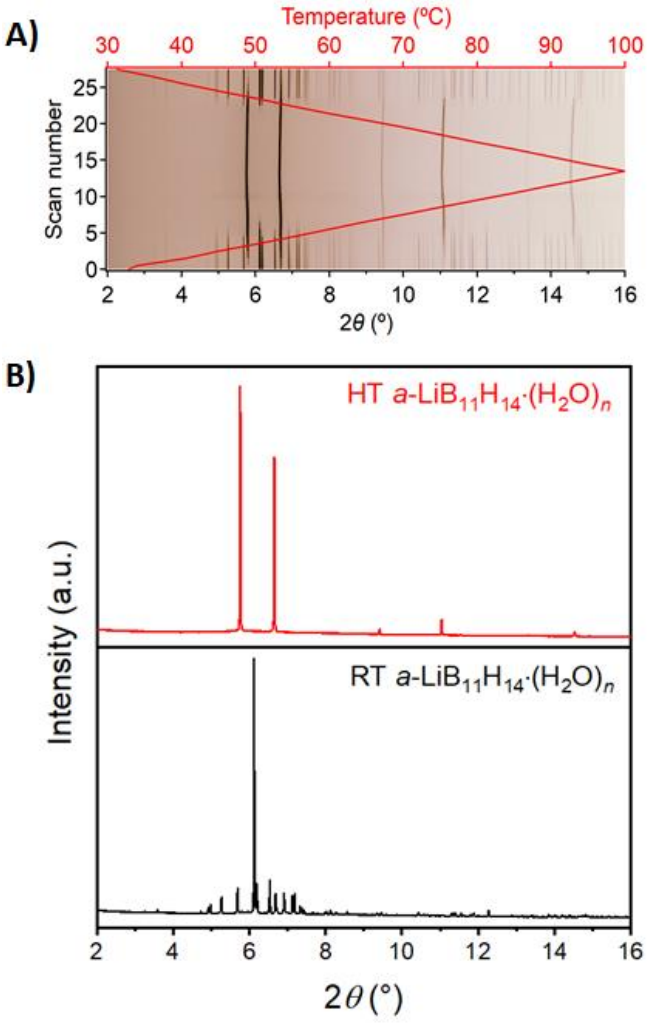

Fig. 2. (A) *In-situ* SR-XRPD data of *a*-$LiB_{11}H_{14}{\cdot}(H_2O)_n$ during heating (5 °C min^{-1}) and cooling (6 °C min^{-1}). A reversible polymorphic phase transition occurs at ≈ 70 °C on heating and at ≈ 55 °C on subsequent cooling. Red line represents temperature. (B) SR-XRPD patterns of HT (high temperature) *a*-$LiB_{11}H_{14}{\cdot}(H_2O)_n$ at 100 °C (red) and RT (room temperature) *a*-$LiB_{11}H_{14}{\cdot}(H_2O)_n$ (black). λ = 0.590827(4) Å.

polymorphic phase change to $Ia\bar{3}d$ (Fig. 2) along with a simultaneous partial melting event. TPPA (Fig. S11), exhibits slight liquification on the surface of the *a*-$LiB_{11}H_{14}\cdot(H_2O)_n$ pellet upon reaching the polymorphic phase change temperature (≈ 70 °C). This is the same melting temperature observed for the salt of $LiB_{11}H_{14}\cdot2H_2O$ (Fig. S7 and S8), which may be related to the presence of 2 water molecules in its crystal structure. *a*-$LiB_{11}H_{14}\cdot(H_2O)_n$ is a mixture of $LiB_{11}H_{14}$ (70 wt.%) with 2 of its hydrates, including only 4.1 wt.% of the monoclinic (*C2/c*) dihydrate, which melts at ≈ 70 °C, but may induce a lower polymorphic phase transition temperature than that seen for dehydrated $LiB_{11}H_{14}$ at 110 °C.[32] Upon heating, *a*-$LiB_{11}H_{14}\cdot(H_2O)_n$ does not lose its solid shape and finally decomposes at 225 °C, which is represented by a sharp exothermic peak, mass loss of 8.4(4)% (Fig. S10) and change in colour (Fig. S11).

XRPD of the fully dehydrated $LiB_{11}H_{14}$ sample shows that this salt exists in an orthorhombic space group *Pbca* identical to the published structure[32] (Fig. S12 and Table S1), while its DSC/TGA plot (Fig. S13) shows an endothermic polymorphic phase change event at 112 °C, also identical to data published previously.[32] The $LiB_{11}H_{14}$ sample also share similar Li^+ conductivity as a function of temperature to published anhydrous $LiB_{11}H_{14}$,[32] as shown below in the 'solid-state ionic conductivity' section (section 3.2). It is important to highlight that the previously published anhydrous $LiB_{11}H_{14}$ was reported to be free of any LiOH or borate impurity meaning that these impurities may not greatly impact the material properties.[32]

Solid-state ionic conductivity

The lithium ion conductivity for each synthesised material was assessed as a function of temperature as illustrated in Fig. 3A. The reported ionic conductivities of dehydrated $LiB_{11}H_{14}$,[32] *b*-$LiB_{11}H_{14}\cdot(H_2O)_n$,[42] and of the ionic liquid electrolyte 1 mol L^{-1} solution of 1-ethyl-3-methylimidazolium tetrafluoroborate ($EMIBF_4$) with lithium tetrafluoroborate ($LiBF_4$),[24] are also displayed for comparison. The EIS measurements for the *a*-$LiB_{11}H_{14}\cdot(H_2O)_n$ sample were performed at discrete isothermal temperatures during four heating and cooling cycles, in order to check the reproducibility of the results and the conditions of the pellet after each experiment, with the results illustrated in Fig. 3B. The Nyquist plots for this sample at 30 and 90 °C, as well as the battery circuit model used to fit this data, are depicted in Fig. S14. Ionic conductivity measurements above 60 °C for sample $LiB_{11}H_{14}\cdot2H_2O$ could not be measured due to melting of the material (Fig. S8), which causes a short circuit in the measurement cell.

Anhydrous $LiB_{11}H_{14}$ exhibits similar Li^+ conductivity to that previously reported for dehydrated $LiB_{11}H_{14}$,[32] which shows that the synthesis of the anhydrous salt was also achieved by a different method. All samples present an ionic conductivity in the order of 10^{-6} S cm^{-1} at 30 °C, but only *a*-$LiB_{11}H_{14}\cdot(H_2O)_n$ reaches an impressive conductivity in the order of 10^{-2} S cm^{-1} at 60 °C due to its polymorphic phase transition. Upon cooling, *a*-$LiB_{11}H_{14}\cdot(H_2O)_n$ maintains its superionic conductivity until ≈ 55 °C, when it reverses back to its RT crystal structure (Fig. 2). Within the temperature range of 60 - 90 °C, *a*-$LiB_{11}H_{14}\cdot(H_2O)_n$ exhibits an ionic conductivity identical to the liquid electrolyte $LiBF_4/EMIBF_4$, making it an ideal candidate for the development of next generation solid-state-batteries. The Nyquist plot at 30 °C (Fig. S14) shows a semi-circle at the high and intermediate frequencies, which is assigned as the sample's charge-transfer resistance, and a spike line (Warburg element) at the low frequency, indicative of Li^+ diffusion.[66] At 90 °C, only the Warburg element can be observed, which indicates a low charge-transfer resistance and a high ionic diffusion.[66–68] Fig. 3B

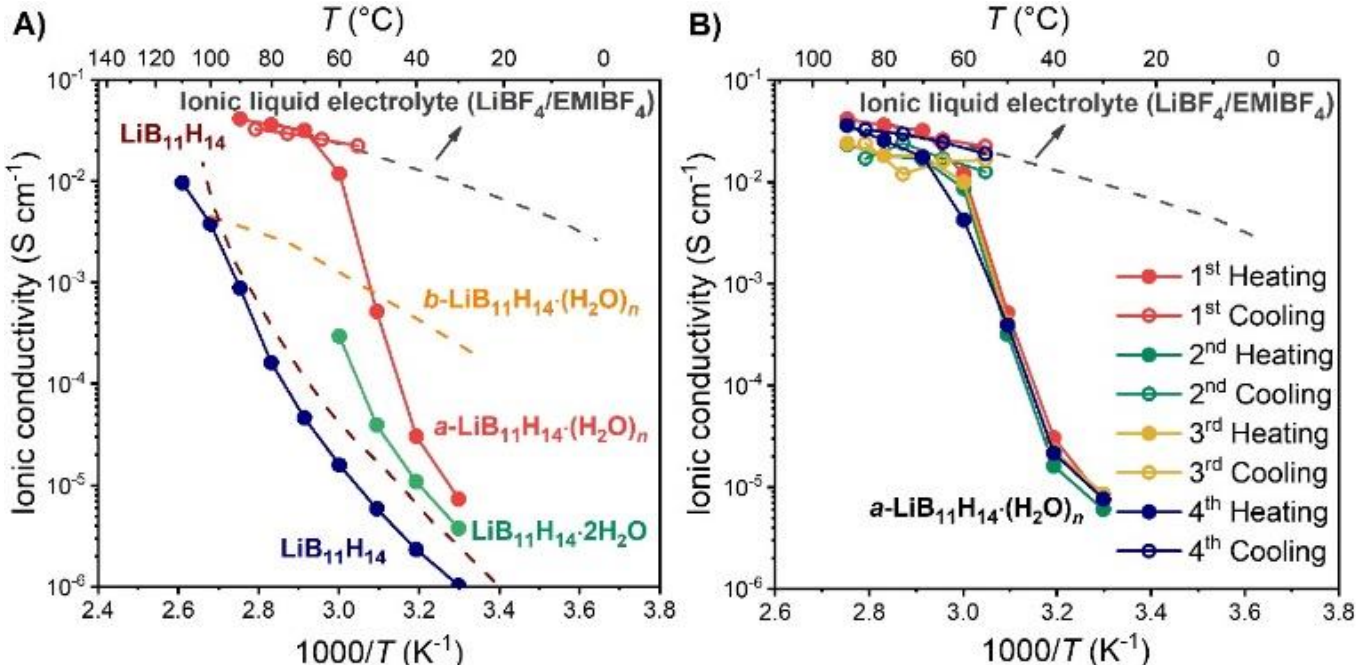

Fig. 3. A) Solid-state ionic conductivity of $LiB_{11}H_{14}\cdot2H_2O$ (green), *a*-$LiB_{11}H_{14}\cdot(H_2O)_n$ (red), and $LiB_{11}H_{14}$ (blue), as a function of temperature. Dehydrated $LiB_{11}H_{14}$ (brown),[32] *b*-$LiB_{11}H_{14}\cdot(H_2O)_n$ (orange),[42] and ionic liquid electrolyte $LiBF_4/EMIBF_4$ (grey)[24] are plotted for comparison. The solid lines denote the ionic conductivity of the materials synthesised in this work. Closed and open symbols represent heating and cooling regimes, respectively. B) Solid-state ionic conductivity of *a*-$LiB_{11}H_{14}\cdot(H_2O)_n$ over four cycles of heating and cooling measurements.

demonstrates that the results of lithium ionic conductivity for *α*-$LiB_{11}H_{14}\cdot(H_2O)_n$ is reproducible after thermally treating the pellet multiple times. The pellet maintained its solid consistency throughout the four cycles, and only small variations on its thickness were measurable, but all within experimental uncertainty (Table S2).

The activation energy required for Li^+ migration for the HT *α*-$LiB_{11}H_{14}\cdot(H_2O)_n$ structure was measured from the slope of the solid-state ionic conductivity plot as 0.16 ± 0.01 eV between 55 and 85 °C (Fig. 3A), which is low compared to other lithium boron-hydrogen materials (Table S3), but the same as that previously reported for HT anhydrous $LiB_{11}H_{14}$ (0.16 eV).[32]

Comparing the results of ionic conductivity of *α*-$LiB_{11}H_{14}\cdot(H_2O)_n$ with other boron-hydrogen salts and mixtures (Fig. S15), *α*-$LiB_{11}H_{14}\cdot(H_2O)_n$ shows similar conductivity trends with temperature as seen for carboranes, such as $LiCB_9H_{10}$.[35] Both compounds present an ionic conductivity in the order of 10^{-6} S cm^{-1} at 30 °C, although conductivity increases significantly to ≈ 10^{-1} S cm^{-1} (superionic conductivity) when the temperature is increased to 90 and 70 °C for $LiCB_9H_{10}$ and *α*-$LiB_{11}H_{14}\cdot(H_2O)_n$, respectively, which also incurs a polymorphic phase change. These superionic results observed for *α*-$LiB_{11}H_{14}\cdot(H_2O)_n$ between 60 and 90 °C also correlate to the results observed for the $0.7Li(CB_9H_{10})$-$0.3Li(CB_{11}H_{12})$ mixture,[35] of which, to date, is the lithium boron-hydrogen sample with the highest ionic conductivity at room temperature (6.7 x 10^{-3} S cm^{-1}). It is important to highlight that carboranes are more expensive and more difficult to synthesise than carbon free boron-hydrogen salts,[44] such as *α*-$LiB_{11}H_{14}\cdot(H_2O)_n$ reported here.

The step-function jump in ionic conductivity due to a polymorphic phase change is also observed in other lithium boron-hydrogen salts, such as $LiBH_4$,[28] Li-7-$CB_{10}H_{13}$,[29] and $LiCB_{11}H_{12}$.[31] Similarly to $LiCB_{11}H_{12}$, *α*-$LiB_{11}H_{14}\cdot(H_2O)_n$ likely assumes a disordered cubic phase at high temperature, which, coupled with the large size and high orientation mobility of the anion, yields a salt with liquid-like ionic conductivity.[31] Besides that, the presence of water in its crystal structure may also assist the Li^+ transport through the high-symmetry cubic polymorph.[41,69] It has already been reported that hydrated $LiBH_4$ can exhibit higher ionic conductivity than anhydrous $LiBH_4$, and that enhancement of Li^+ conduction might be associated to the motion of structural water.[41] In a similar manner, the presence of ammonia molecules in hemi-ammine lithium borohydride ($LiBH_4\cdot1/2NH_3$) assists the migration of Li^+ through the crystal structure, increasing its ionic conductivity.[43]

The sample of *β*-$LiB_{11}H_{14}\cdot(H_2O)_n$ presents a cubic $Fm\bar{3}m$ space group at room temperature,[42] however it does not reach such high Li^+ conductivity (close to 10^{-1} S cm^{-1}) as *α*-$LiB_{11}H_{14}\cdot(H_2O)_n$ even at high temperatures. This might be related to the fact that sample *α*-$LiB_{11}H_{14}\cdot(H_2O)_n$ exhibits a small quantity of the molten $LiB_{11}H_{14}\cdot2H_2O$ phase and a disordered HT polymorph above 60 °C, which significantly enhances its ionic conductivity. It is also hypothesised that the salt *β*-$LiB_{11}H_{14}\cdot(H_2O)_n$ may exhibit disordered structural behaviour in its cubic polymorph at room temperature and might undergo a polymorphic phase transition to a more ordered crystal structure at sub-zero temperatures.[42]

In order to further investigate any possible order-disorder phase transition and to assess the information concerning structural dynamics (including rotations/reorientations of boron cages) *in-situ* SR-XRPD and ^{11}B spin-lattice NMR relaxation rates (T_1^{-1}) of *β*-$LiB_{11}H_{14}\cdot(H_2O)_n$ were measured as a function of temperature. The *in-situ* SR-XRPD results are displayed in Fig. S16 when cooling from RT to -175 °C, and there is no clear evidence of a polymorphic transition, nor in the NMR data when the sample is cooled. Boron spin-lattice relaxation in NMR data is influenced by fluctuations in dipolar interactions of boron nuclei with other boron atoms, protons, and Li nuclei, as well as by fluctuations of the interaction between the nuclear quadrupole moment of boron nuclei and the electric field gradient tensor (EFG) at the site of the nuclei. These fluctuations are caused by the motions of the units. As the relaxation rate increases with temperature, the same approach is followed as previously reported[70] to understand the dynamic processes in *β*-$LiB_{11}H_{14}\cdot(H_2O)_n$. It is found that there are two contributions from two types of dynamic processes, assuming the asymptotic form of the simple relaxation model and an additional temperature-independent contribution to relaxation due to paramagnetic impurities that are present in the sample. The dynamic process with the higher activation energy, E_{a1} = 0.32(1) eV, is associated with thermally-activated rotations/reorientations of the boron cages, and is in line with the activation energies for similar systems.[29,70–72] This activation energy is lower than the one obtained from ionic conductivity for this sample (0.5 eV),[42] however this is expected, as a jump of Li^+ also includes some breaking of the lattice, which requires additional energy.[30] The process with the lower activation energy, E_{a2} = 0.074(5) eV, is likely associated with tumbling or twitching of a small fraction of loosely-bound $B_{11}H_{14}^-$ units in the system, and the activation energy is similar to what has been previously observed for that type of dynamic process in $Ag_2B_{12}H_{12}$.[70]

Electrochemical stability

The oxidative stability limit of *α*-$LiB_{11}H_{14}\cdot(H_2O)_n$ against Li metal was determined through a linear sweep voltammetry experiment at 30 °C following the method proposed by Asakura *et al*.[73] The voltammogram shows two oxidation onsets (Fig. S17), a minor event at 2.1 V and another more significant oxidation event at 2.8 V, which is in agreement with results previously published for *β*-$LiB_{11}H_{14}\cdot(H_2O)_n$.[42] The first oxidation onset is low in intensity and may be due to the background current, which is a non-faradaic current attributed to the double-layer capacitance,[73] rather than an onset of decomposition of the material. A similar voltammogram is observed for a previously reported solid-mixture of $LiB_{11}H_{14}$:$LiB_{11}H_{13}R'$ (*R'* = OH and $OB_{11}H_{13}Li$),[32] which presents a steep background current prior to its Faradaic oxidative current at 2.52 V. Besides that, the solid-solution $Li_2(B_{11}H_{14})(CB_{11}H_{12})$ also exhibits an onset of decomposition at ≈ 2.6 V,[32] similar to other *nido*-boranes, such as $NaB_{11}H_{14}$[74] and $NaB_{11}H_{14}\cdot(H_2O)_n$[42] that exhibit an oxidative current of 2.6 V vs. Na/Na^+. Therefore, *α*-$LiB_{11}H_{14}\cdot(H_2O)_n$ exhibits a similar oxidative stability limit of 2.8 V against Li/Li^+. The small peak current (≈ 4.0 μA cm^{-2}) during oxidation indicates that only a small amount of *α*-$LiB_{11}H_{14}\cdot(H_2O)_n$

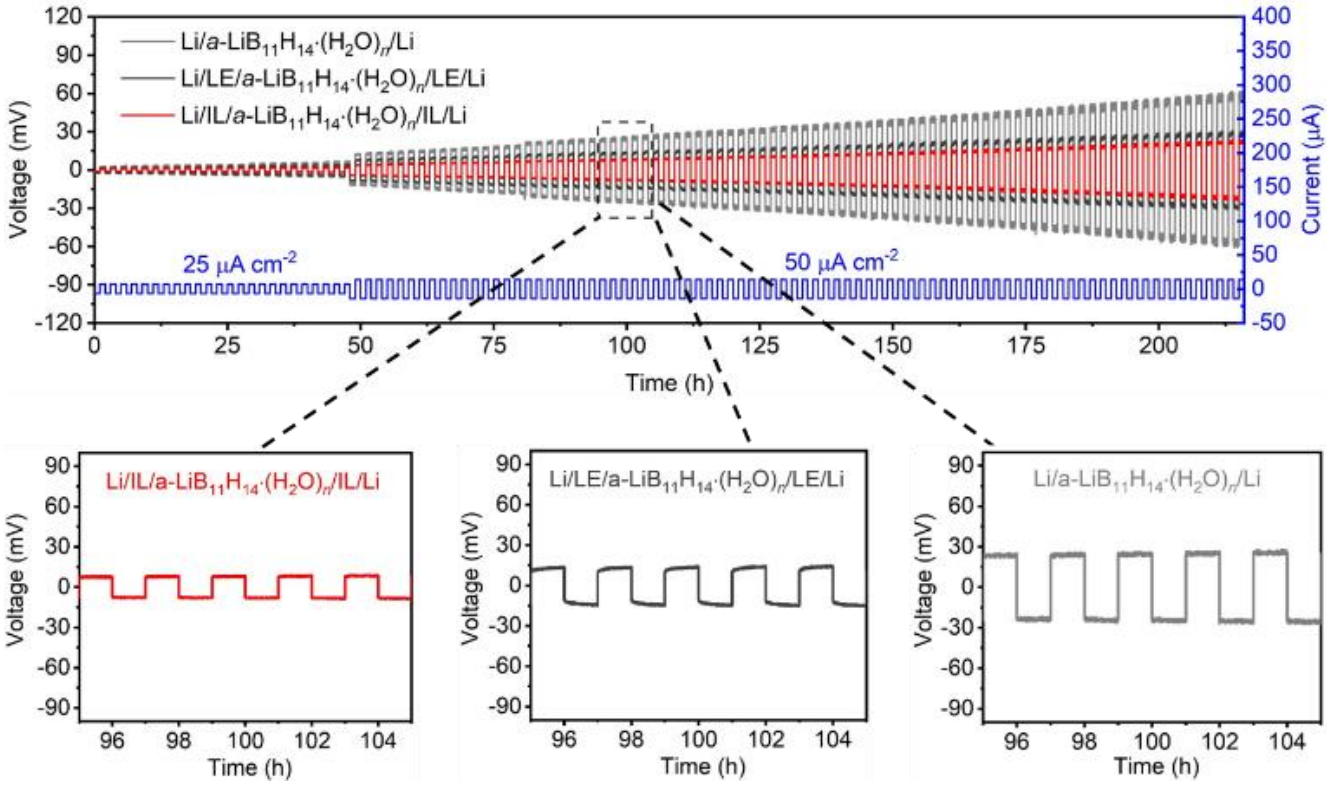

Fig. 4. Galvanostatic cycling profiles at 60 °C with a current density of 25 and 50 μA cm^{-2} for 1 h in each direction of a Li/*a*-$LiB_{11}H_{14}\cdot(H_2O)_n$/Li coin cell (grey), Li/LE/*a*-$LiB_{11}H_{14}\cdot(H_2O)_n$/LE/Li Swagelok-type cell (black), and Li/IL/*a*-$LiB_{11}H_{14}\cdot(H_2O)_n$/IL/Li Swagelok-type cell (red), where LE stands for liquid electrolyte (1.0 M $LiPF_6$ EC/DMC) and IL is ionic liquid ($LiB_{11}H_{14}\cdot 2H_2O$).

was oxidised, and the presence of a small onset in the same region near 2.8 V during the second LSV cycle (Fig. S17), might indicate a further oxidation of its surface layer.[75] It is important to highlight that this reaction is an event that occurs on the interface electrode/electrolyte, thus the bulk stability of *a*-$LiB_{11}H_{14}\cdot(H_2O)_n$ might be preserved, as it has already been observed for other *nido*-boranes.[42]

The electrochemical stability of *a*-$LiB_{11}H_{14}\cdot(H_2O)_n$ against lithium metal was also evaluated through galvanostatic cycling of three different types of symmetric cells at 60 °C. Initially, a pellet of *a*-$LiB_{11}H_{14}\cdot(H_2O)_n$ was prepared and assembled between Li disks in a coin cell to form a Li/*a*-$LiB_{11}H_{14}\cdot(H_2O)_n$/Li configuration. However, the insufficient contact between Li and solid electrolyte can form voids at the interface, which increases interfacial resistance and overpotential that is required to generate and maintain a constant current.[4,76] One way to increase surface contact and reduce the magnitude of the overpotential upon cycling is by applying a continuous stack pressure to the cell.[76,77] An alternative strategy is to utilise a wetting agent, such as an ionic liquid, between the solid electrolyte and the Li metal interface.[17] Even the type of battery (e.g. coin cell or a Swagelok cell) that is used to conduct the experiments can influence the results of interfacial resistance.[78] In this work, a second symmetric cell of Li/*a*-$LiB_{11}H_{14}\cdot(H_2O)_n$/Li was prepared with the addition of a drop of liquid electrolyte (LE, 1.0 M $LiPF_6$ EC/DMC) between the interfaces of the lithium metal and the SSE to form a Li/LE/*a*-$LiB_{11}H_{14}\cdot(H_2O)_n$/LE/Li configuration. A third symmetric cell was also prepared with the addition of a small amount (1 mg) of $LiB_{11}H_{14}\cdot 2H_2O$ on the interface between Li/SSE in order to evaluate the properties of $LiB_{11}H_{14}\cdot 2H_2O$ as an ionic liquid as it melts at ≈ 60 °C. This cell configuration is here referred to as Li/IL/*a*-$LiB_{11}H_{14}\cdot(H_2O)_n$/IL/Li. Both hybrid solid/liquid cells were prepared in a Swagelok-type assembly, as this set-up provides a slightly higher stack pressure, even though small, than for a coin cell.

The results for galvanostatic cycling of the symmetric cells at 60 °C are displayed in Fig. 4, where it is possible to observe the reversibility of Li plating/stripping for 108 cycles with a flat polarisation (no side reactions can be observed) in all different cells used for this study.

The results in Fig. 4 demonstrate that the overpotential for all cells increases upon cycling, however the magnitude of the overpotential for the cell with ionic liquid ($LiB_{11}H_{14}\cdot 2H_2O$) is the smallest, being 21 mV after 216 h cycling (48 h at 25 μA cm^{-2} and 168 h at 50 μA cm^{-2}) compared to the cells with a LE (≈ 27 mV after 48 h at 25 μA cm^{-2} and 168 h at 50 μA cm^{-2}) and without an additive in a coin cell (≈ 55 mV after 48 h at 25 μA cm^{-2} and 168 h at 50 μA cm^{-2}). This indicates that in the absence of an effective stack pressure set-up, the use of a Swagelok-type cell instead of a coin cell and addition of an ionic liquid or liquid electrolyte can improve the stability of Li/SSE,[17] and that $LiB_{11}H_{14}\cdot 2H_2O$ works effectively as a wetting agent for this purpose.

An endurable time control measurement was performed with a Li symmetric cell of *a*-$LiB_{11}H_{14}\cdot(H_2O)_n$ (Li/*a*-$LiB_{11}H_{14}\cdot(H_2O)_n$/Li) to evaluate its chemical stability against Li metal and to identify its critical current density (CCD). The cell was analysed from 25 to 775 μA cm^{-2} for 30 min sweeps during 5 hours at each current

with the step gap of 25 μA cm^{-2} (Fig. S18). The voltage increases with increase of current density, however no major changes can be detected during cycling at each current. Polarisation can be observed as the current density reaches 500 μA cm^{-2}, which might be attributed to an increased contact loss between Li/SSE that occurs during lithium striping/plating leading to enhanced interfacial resistance.[79] A short circuit can be identified at the current density of 775 μA cm^{-2}, which determines the CCD to be 750 μA cm^{-2} at 60 °C. This is a similar result to what is observed for Ga-doped $Li_7La_3Zr_2O_{12}$ (700 μA cm^{-2} at 27 °C)[80] and higher than what was estimated for $Li_2(B_{11}H_{14})(CB_{11}H_{12})$ (160 μA cm^{-2} at 60 °C).[32]

The electrode/electrolyte interfacial resistances (R_{SEI}) for the systems Li/IL/*a*-$LiB_{11}H_{14}\cdot(H_2O)_n$/IL/Li and Li/*a*-$LiB_{11}H_{14}\cdot(H_2O)_n$/Li were calculated after a 1 hour isothermal equilibrium at 60 °C based on the fitting of the Nyquist plots (Fig. S19) with the equivalent circuit model (Fig. S14A). As the capacitance components for both systems are in the order of 10^{-6} F, the value of the parallel resistance component is attributed to the contact surface resistance.[81] In order to obtain the final result of interfacial resistance, the resistance is divided in half, as both interfaces are equivalent, and normalised by the surface area.[4,35,81,82] The results are presented in Table S4. The interfacial resistance was calculated to be 3.6 Ω cm^2 (± 0.2) for the system containing ionic liquid and 4.4 Ω cm^2 (± 0.3) for the system with bare SSE/Li. Even though the initial difference in interfacial resistance is small, over time and with the application of a current, the overpotential (and thus interfacial resistance) increases at a higher rate for the system that does not contain a wetting agent and is assembled in a coin cell (Fig. 4). Despite the growth in interfacial resistance seen in Fig. 4 the magnitude of interfacial resistance is still small,[12] which makes *a*-$LiB_{11}H_{14}\cdot(H_2O)_n$ coupled with $LiB_{11}H_{14}\cdot 2H_2O$ promising materials for lithium ion technology applications.

Battery test

The electrochemical properties of *a*-$LiB_{11}H_{14}\cdot(H_2O)_n$ as a solid-state electrolyte (SSE) were also evaluated in a solid-liquid hybrid battery with a mixture of TiS_2 (active cathode material with a high electronic conductivity) with the SSE as a cathode, Li metal as the anode, and a coating of a drop of LE (1.0 M $LiPF_6$ EC/DMC) on the side of Li/SSE to reduce interfacial resistance (Fig. 5A). Titanium disulphide is a known solid cathode material with a layered structure that has the ability to favourably intercalate and store Li ions with minor lattice expansion.[83–85] Moreover, it presents high electronic conductivity, low weight and relatively low cost, which makes it suitable for battery studies.[83–85] With the superionic conductivity exhibited by *a*-$LiB_{11}H_{14}\cdot(H_2O)_n$ at 60 °C (1.2 x 10^{-2} S cm^{-1}), this temperature was selected to perform all battery tests. The cell Li/LE/*a*-$LiB_{11}H_{14}\cdot(H_2O)_n$/*a*-$LiB_{11}H_{14}\cdot(H_2O)_n$+$TiS_2$ was cycled at different *C*-rates, from 0.05 to 0.4 *C* (1 *C* = 239 mA g^{-1}) in the voltage range 1.7 – 2.5 V, and reversible charge-discharge profiles can be observed (Fig. 5B). The *C*-rate is here defined as *nC*, in which the current fully discharges and charges the battery in 1/*n* hours. The discharge capacity in the first cycle was 190 mAh g^{-1}, which corresponds to 79% of the theoretical gravimetric energy storage capacity of TiS_2 (239 mAh g^{-1}), the same observed when using $Li_2(B_{11}H_{14})(CB_{11}H_{12})$ as an SSE.[32] With the increase of *C*-rate from 0.05 *C* by 2, 4, 6 and 8 times, the capacity retention of the battery dropped to 72, 69, 67 and 65%, respectively (Fig. 5C), which is expected, as there is an increase in current density. The battery was then cycled 50 more times at the highest *C*-rate (0.4 *C* = 95.6 mA g^{-1}) (Fig. 5D), and the cell retained 83% of its capacity shown in the first cycle at 0.4 *C* (156 mAh g^{-1}), which corresponds to a retention of 68% of the first discharge capacity obtained at 0.05 *C* (190 mAh g^{-1}). Fig. 5E shows that similar discharge capacity of 200 mAh g^{-1} was obtained at 0.1 *C* in the first cycle, and the cell retained 84% of this initial capacity after 5 more cycles at 0.1 *C*. At the 7th cycle, *C*-rate was doubled, and a slight drop of specific capacity occurred, which is expected with *C*-rate increase. After 60 cycles at 0.2 *C*, the cell retained 82% of its capacity from its first cycle at this *C*-rate (162 mAh g^{-1}). A similar result is observed for the battery containing the SSE composite $LiBH_4$-MgO, which holds more than 80% capacity after 65 cycles at 60 °C, however at the lower *C*-rate of 0.05 *C*.[4] The retained capacity obtained here is slightly lower than the one observed for a $Li_2(B_{11}H_{14})(CB_{11}H_{12})$ SSE, which exhibits a retention capacity of ≈ 84% (from the 6th cycle) after 100 cycles.[32] Nevertheless, it is important to highlight that the experiment with $Li_2(B_{11}H_{14})(CB_{11}H_{12})$ was conducted with a continuous stack pressure to the cell.[32] Cycling causes morphological changes at the interface of the electrode/electrolyte, which leads to loss of contact and reduces the performance and stability of a solid-state battery.[4,76] The addition of the liquid electrolyte between Li and SSE reduces its interfacial resistance but it still does increase upon cycling. When high external pressures are applied to the cell, more contact can be maintained between electrode/electrolyte that may be more effective than just adding a wetting agent to the interface.[86] Fig. 5E also shows that the cell of Li/LE/*a*-$LiB_{11}H_{14}\cdot(H_2O)_n$/*a*-$LiB_{11}H_{14}\cdot(H_2O)_n$+$TiS_2$ exhibited a Coulombic efficiency of ≈ 98% during the first 6 cycles, and it slightly increased to 99% after shifting to a higher *C*-rate, keeping this Coulombic efficiency for the rest of the experiment.

A battery of Li/IL/*a*-$LiB_{11}H_{14}\cdot(H_2O)_n$/IL/*a*-$LiB_{11}H_{14}\cdot(H_2O)_n$+$TiS_2$ was also prepared (IL instead of LE wetting agent) and had its electrochemical properties evaluated in the same way as the cell containing LE. Based on the results presented in Fig. S20, it is possible to observe reversible charge-discharge cycling and that the discharge capacity in the first cycle at 0.05 *C* (194 mAh g^{-1}) was similar to the one observed for the cell with LE. This corresponds to 81% of theoretical capacity of TiS_2 (239 mAh g^{-1}). However, the increase of *C*-rate from 0.05 *C* by 2, 4, 6 and 8 times causes the capacity retention of the battery to drop to 59, 46, 39 and 34%, respectively (Fig. S20B), which indicates a much lower performance than when the battery is prepared with the addition of LE (Fig. S20C). When the cell is cycled only at 0.4 *C* (Fig. S20D), its discharge capacity in the first cycle was 186 mAh g^{-1}, which corresponds to 78% of the theoretical capacity of TiS_2 (239 mAh g^{-1}), and it drops to 63 mAh g^{-1} in the 50th cycle, which means that the capacity retention was only 34% from its first cycle.

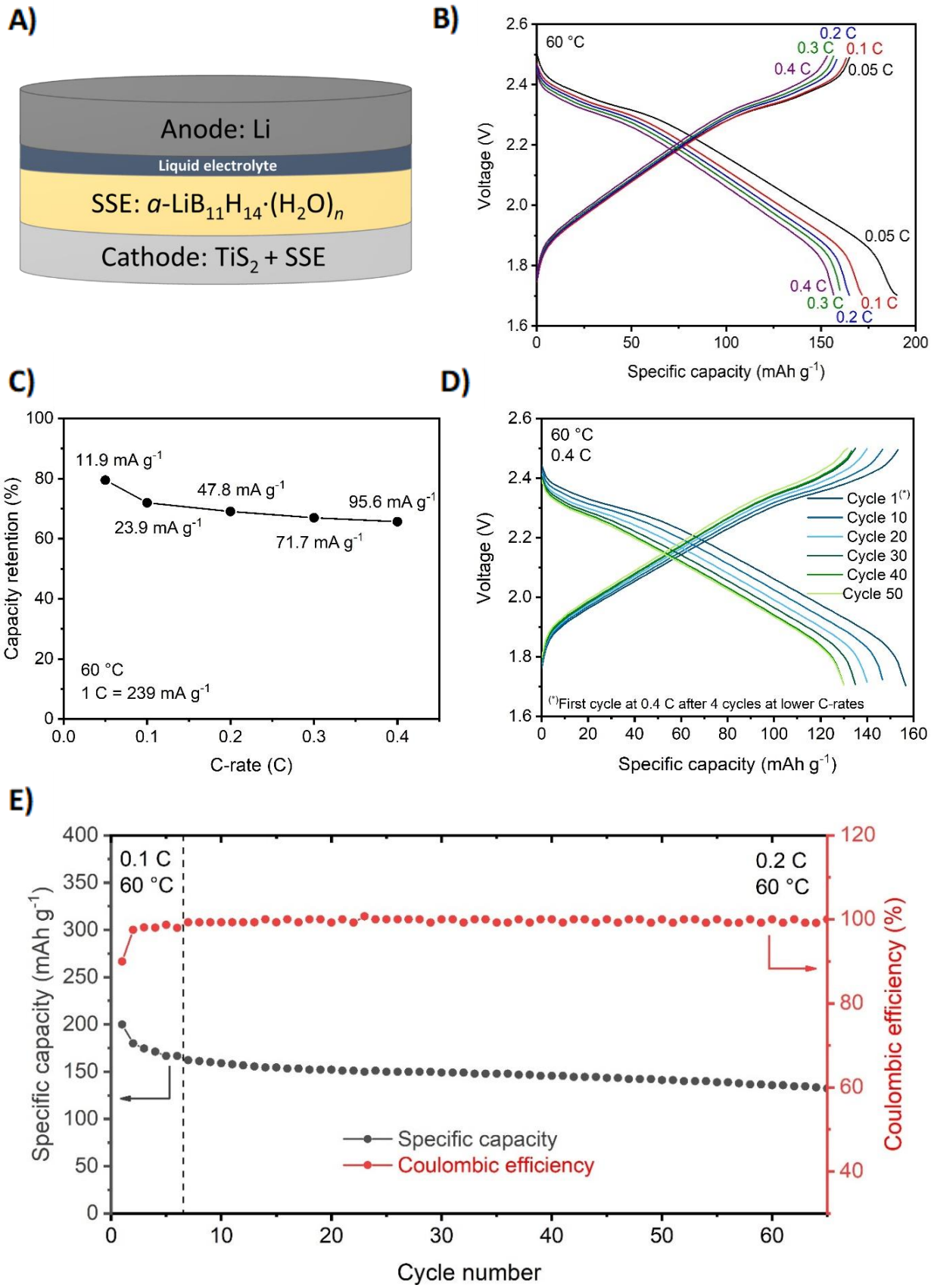

Fig. 1. A) Schematic representation of the solid-state battery Li/LE/α-$LiB_{11}H_{14}\cdot(H_2O)_n$/$\alpha$-$LiB_{11}H_{14}\cdot(H_2O)_n$+$TiS_2$ in a Swagelok-type cell. B) Discharge/charge profiles at 0.05, 0.1, 0.2, 0.3 and 0.4 *C* (1.7 – 2.5 V) at 60 °C. C) Capacity retention at different *C*-rates. D) Discharge/charge profiles at 0.4 *C* for 50 cycles at 60 °C after being initially cycled at 0.05, 0.1, 0.2 and 0.3 *C*. E) Coulombic efficiency and discharge specific capacity at 0.1 *C* for the first 6 cycles and at 0.2 *C* from the 7th to the 65th

The addition of $LiB_{11}H_{14}\cdot 2H_2O$ at the interface of SSE/Li is a good strategy to reduce interfacial resistance and overpotential during cycling (Fig. 4), however it does not improve the performance of the battery as much as a traditional LE wetting agent when TiS_2 is used as the cathode (Fig. S20). This may be related to some instability or reactivity between $LiB_{11}H_{14}\cdot 2H_2O$ and TiS_2, but other types of cathode materials, such as sulphur[35] or oxide cathodes,[27,81,87] should be investigated to analyse their suitability. The preparation of a cell with the application of $LiB_{11}H_{14}\cdot 2H_2O$ only at the SSE/Li interface should also be assessed. Surface chemistry analyses should also be conducted to assess the interface Li/SSE after lithium striping/plating. Experiments to improve the battery performance of *a*-$LiB_{11}H_{14}\cdot(H_2O)_n$ should be considered for further studies with the application of a stack pressure combined with the use of an ionic liquid or liquid electrolyte in the interface SSE/Li and SSE/cathode. This would increase the interfacial contact and hence aid capacity retention. Further research on the application of *a*-$LiB_{11}H_{14}\cdot(H_2O)_n$ with the use of sulphur as the cathode, for example, should also be considered due to the increased energy density (1672 mAh g^{-1}) and applicable working voltage (2.1 V vs Li^+/Li)[35] of this electrode with *a*-$LiB_{11}H_{14}\cdot(H_2O)_n$ as SSE.

Conclusions

A low cost synthesis of hydrated and anhydrous $LiB_{11}H_{14}$ salts is presented. It was observed that the salt $LiB_{11}H_{14}\cdot 2H_2O$ consists of a new class of ionic liquid, as it melts at ≈ 70 °C. The sample *a*-$LiB_{11}H_{14}\cdot(H_2O)_n$ undergoes a polymorphic phase transition at the same temperature and assumes a HT polymorph with a cubic $Ia\bar{3}d$ space group and superionic conductivity (3.2 x 10^{-2} S cm^{-1} at 70 °C). Hence, the water content in the $LiB_{11}H_{14}$ salt seems to be a good strategy to tune the thermal and ionic conductivity properties. *a*-$LiB_{11}H_{14}\cdot(H_2O)_n$ also shows an oxidative stability limit of 2.8 V against Li^+/Li and reversible Li plating/stripping for at least 216 hours cycling.

The material $LiB_{11}H_{14}\cdot 2H_2O$ worked effectively as an ionic liquid additive to the interface between lithium and solid state electrolyte at 60 °C in a Swagelok-type cell as it significantly reduced the magnitude of the overpotential (and thus interfacial resistance) upon cycling. However, it was not enough to completely resolve the overpotential issue during lithium striping/plating. Further optimisation is required, such as the application of an external pressure to increase interfacial contact, for future SSE research. The use of $LiB_{11}H_{14}\cdot 2H_2O$ as an ionic liquid in the interface SSE/electrode did not demonstrate good performance with TiS_2 as a battery cathode. However, its application should be investigated against other types of cathode materials and electrolytes. The use of the liquid electrolyte 1.0 M $LiPF_6$ EC/DMC (*v/v* = 50/50) as a wetting agent in the solid-liquid hybrid cell was more efficient and exhibited good performance.

Despites the high temperature required (60 °C) for the use of *a*-$LiB_{11}H_{14}\cdot(H_2O)_n$ as SSE, the promising features this salt exhibits, such as, liquid-like ionic conductivity, relatively high oxidative stability limit vs Li metal, cyclability against Li metal anode and TiS_2 cathode, and a facile low cost synthesis, make it an important contribution for future hydridoborate SSE research. The variation of water content in the crystal structure can also be considered a novel strategy to tune ionic conductivity properties and to perhaps obtain a SSE with enhanced properties at RT in the future. The application of a liquid electrolyte or an ionic liquid at the interface SSE/electrode with the use of an apparatus that provides an external pressure seems to be a good strategy to increase performance of the battery with *a*-$LiB_{11}H_{14}\cdot(H_2O)_n$ as SSE.

Conflicts of interest

There are no conflicts to declare.

Acknowledgements

DHPS acknowledges the support from Curtin-ATN South American Scholarship and Tuition Fee-Offset Scholarship through Curtin University. CEB, MP, and TDH acknowledge the financial support of the Global Innovation Linkage (GIL73589). CEB acknowledges the financial support of the ARC for the LIEF grant LE170100199. AG acknowledges the funding of the Slovenian Research Agency, basic core funding grants P1-0125 and P2-0209. This research was undertaken on the Powder Diffraction beamline at the Australian Synchrotron, part of ANSTO. The authors thank Dr Gareth Nealon for his help in solid-state NMR data collection and Dr Thomas Becker for his help in the Raman experiment.

References

1 F. Zheng, M. Kotobuki, S. Song, M. O. Lai and L. Lu, J. Power Sources, 2018, 389, 198–213.
2 Y. Nishi, J. Power Sources, 2001, 100, 101–106.
3 H. W. Kim, P. Manikandan, Y. J. Lim, J. H. Kim, S. Nam and Y. Kim, J. Mater. Chem. A, 2016, 4, 17025–17032.
4 V. Gulino, M. Brighi, F. Murgia, P. Ngene, P. De Jongh, R. Černý and M. Baricco, ACS Appl. Energy Mater., 2021, 4, 1228–1236.
5 S. Kim, K. Kisu, S. Takagi, H. Oguchi and S. Orimo, ACS Appl. Energy Mater., 2020, 3, 4831–4839.
6 L. Han, M. L. Lehmann, J. Zhu, T. Liu, Z. Zhou, X. Tang, C. Te Heish, A. P. Sokolov, P. Cao, X. C. Chen and T. Saito, Front. Energy Res., 2020, 8, 1–19.
7 H. Zhang, C. Li, M. Piszcz, E. Coya, T. Rojo, L. M. Rodriguez-Martinez, M. Armand and Z. Zhou, Chem. Soc. Rev., 2017, 46, 797–815.
8 Z. Ding, J. Li, J. Li and C. An, J. Electrochem. Soc., 2020, 167, 070541.
9 H. Kim, G. Jeong, Y.U. Kim, J.H. Kim, C.M. Park and H.J. Sohn, Chem. Soc. Rev., 2013, 42, 9011–9034.
10 Z. Lu and F. Ciucci, Chem. Mater., 2017, 29, 9308–9319.
11 A. Manthiram, X. Yu and S. Wang, Nat. Rev. Mater., 2017, 2, 1–16.
12 Z. Jiang, Q. Han, S. Wang and H. Wang, ChemElectroChem, 2019, 6, 2970–2983.
13 X. Pan, L. Liu, P. Yang, J. Zhang and M. An, Solid State Ionics, 2020, 357, 115466.
14 T. Kim, D.Y. Son, L. K. Ono, Y. Jiang and Y. Qi, J. Phys. D. Appl. Phys., 2021, 54, 475501.

15 J. Tang, L. Wang, L. You, X. Chen, T. Huang, L. Zhou, Z. Geng and A. Yu, ACS Appl. Mater. Interfaces, 2021, 13, 2685–2693.
16 J. Zheng, M. Gu, H. Chen, P. Meduri, M. H. Engelhard, J.G. Zhang, J. Liu and J. Xiao, J. Mater. Chem. A, 2013, 1, 8464–8470.
17 B. Zheng, J. Zhu, H. Wang, M. Feng, E. Umeshbabu, Y. Li, Q.H. Wu and Y. Yang, ACS Appl. Mater. Interfaces, 2018, 10, 25473–25482.
18 H. Huo, N. Zhao, J. Sun, F. Du, Y. Li and X. Guo, J. Power Sources, 2017, 372, 1–7.
19 K.W. Kim, H. W. Kim, Y. Kim and J.K. Kim, Electrochim. Acta, 2017, 236, 394–398.
20 N. M. Asl, J. Keith, C. Lim, L. Zhu and Y. Kim, Electrochim. Acta, 2012, 79, 8–16.
21 C. Wang, Q. Sun, Y. Liu, Y. Zhao, X. Li, X. Lin, M. N. Banis, M. Li, W. Li, K. R. Adair, D. Wang, J. Liang, R. Li, L. Zhang, R. Yang, S. Lu and X. Sun, Nano Energy, 2018, 48, 35–43.
22 X. Han, Y. Gong, K. Fu, X. He, G. T. Hitz, J. Dai, A. Pearse, B. Liu, H. Wang, G. Rubloff, Y. Mo, V. Thangadurai, E. D. Wachsman and L. Hu, Nat. Mater., 2017, 16, 572–579.
23 V. Thangadurai, S. Narayanan and D. Pinzaru, Chem. Soc. Rev., 2014, 43, 4714–4727.
24 N. Kamaya, K. Homma, Y. Yamakawa, M. Hirayama, R. Kanno, M. Yonemura, T. Kamiyama, Y. Kato, S. Hama, K. Kawamoto and A. Mitsui, Nat. Mater., 2011, 10, 682–686.
25 J. Lau, R. H. DeBlock, D. M. Butts, D. S. Ashby, C. S. Choi and B. S. Dunn, Adv. Energy Mater., 2018, 8, 1800933.
26 Q. Zhang, D. Cao, Y. Ma, A. Natan, P. Aurora and H. Zhu, Adv. Mater., 2019, 31, 1901131.
27 F. Lu, Y. Pang, M. Zhu, F. Han, J. Yang, F. Fang, D. Sun, S. Zheng and C. Wang, Adv. Funct. Mater., 2019, 29, 1809219.
28 M. Matsuo, Y. Nakamori, S. Orimo, H. Maekawa and H. Takamura, Appl. Phys. Lett., 2007, 91, 224103.
29 W. S. Tang, M. Dimitrievska, V. Stavila, W. Zhou, H. Wu, A. A. Talin and T. J. Udovic, Chem. Mater., 2017, 29, 10496–10509.
30 W. S. Tang, M. Matsuo, H. Wu, V. Stavila, W. Zhou, A. A. Talin, A. V Soloninin, R. V Skoryunov, O. A. Babanova, A. V Skripov, A. Unemoto, S.I. Orimo and T. J. Udovic, Adv. Energy Mater., 2016, 6, 1502237.
31 W. S. Tang, A. Unemoto, W. Zhou, V. Stavila, M. Matsuo, H. Wu, S. Orimo and T. J. Udovic, Energy Environ. Sci., 2015, 8, 3637–3645.
32 S. H. Payandeh, D. Rentsch, Z. Łodziana, R. Asakura, L. Bigler, R. Černý, C. Battaglia and A. Remhof, Adv. Funct. Mater., 2021, 31, 2010046.
33 P. E. de Jongh, D. Blanchard, M. Matsuo, T. J. Udovic and S. Orimo, Appl. Phys. A Mater. Sci. Process., 2016, 122, 251.
34 R. Mohtadi and S. I. Orimo, Nat. Rev. Mater., 2016, 2, 1–16.
35 S. Kim, H. Oguchi, N. Toyama, T. Sato, S. Takagi, T. Otomo, D. Arunkumar, N. Kuwata, J. Kawamura and S. Orimo, Nat. Commun., 2019, 10, 1–9.
36 Y. S. Choi, Y.S. Lee, K. H. Oh and Y. W. Cho, Phys. Chem. Chem. Phys., 2016, 18, 22540–22547.
37 V. Gulino, L. Barberis, P. Ngene, M. Baricco and P. E. De Jongh, ACS Appl. Energy Mater., 2020, 3, 4941–4948.
38 Y. S. Choi, Y. S. Lee, D. J. Choi, K. H. Chae, K. H. Oh and Y. W. Cho, J. Phys. Chem. C, 2017, 121, 26209–26215.
39 M. Matsuo, A. Remhof, P. Martelli, R. Caputo, M. Ernst, Y. Miura, T. Sato, H. Oguchi, H. Maekawa, H. Takamura, A. Borgschulte, A. Züttel and S. Orimo, J. Am. Chem. Soc., 2009, 131, 16389–16391.
40 D. Sveinbjörnsson, J. S. G. Myrdal, D. Blanchard, J. J. Bentzen, T. Hirata, M. B. Mogensen, P. Norby, S.I. Orimo and T. Vegge, J. Phys. Chem. C, 2013, 117, 3249–3257.
41 A. Takano, I. Oikawa, A. Kamegawa and H. Takamura, Solid State Ionics, 2016, 285, 47–50.
42 D. H. P. Souza, K. T. Møller, S. A. Moggach, T. D. Humphries, A. M. D'Angelo, C. E. Buckley and M. Paskevicius, J. Mater. Chem. A, 2021, 9, 15027–15037.
43 Y. Yan, J. B. Grinderslev, Y.S. Lee, M. Jørgensen, Y. W. Cho, R. Černý and T. R. Jensen, Chem. Commun., 2020, 56, 3971–3974.
44 A. Berger, C. E. Buckley and M. Paskevicius, Inorg. Chem., 2021, 60, 14744–14751.
45 B. Ringstrand, D. Bateman, R. K. Shoemaker and Z. Jano-user, Collect. Czechoslov. Chem. Commun., 2009, 74, 419–431.
46 A. Hepp, R. Labbow, F. Reiß, A. Schulz and A. Villinger, Eur. J. Inorg. Chem., 2018, 2018, 2905–2914.
47 D. Reed and D. Book, Curr. Opin. Solid State Mater. Sci., 2011, 15, 62–72.
48 L. A. Leites, Chem. Rev., 1992, 92, 279–323.
49 D. Sethio, L. M. Lawson Daku and H. Hagemann, Int. J. Hydrogen Energy, 2017, 42, 22496–22501.
50 S. Najiba and J. Chen, Proc. Natl. Acad. Sci. U. S. A., 2012, 109, 19140–19144.
51 M. Silva, E. F. O'Bannon and Q. Williams, Am. Mineral., 2018, 103, 1306–1318.
52 Z. Yongquan, F. Chunhui, F. Yan and Z. H. U. Fayan, Chinese J. Chem. Eng., 2013, 21, 1048–1056.
53 D. Maniua, T. Iliescu, I. Ardelean, S. Cinta-Pinzaru, N. Tarcea and W. Kiefer, J. Mol. Struct., 2003, 651–653, 485–488.
54 B. N. Meera and J. Ramakrishna, J. Non. Cryst. Solids, 1993, 159, 1–21.
55 E. L. Muetterties, J. H. Balthis, Y. T. Chia, W. H. Knoth and H. C. Miller, Inorg. Chem., 1964, 3, 444–451.
56 Z. Huang, M. Eagles, S. Porter, E. G. Sorte, B. Billet, R. L. Corey, M. S. Conradi and J. C. Zhao, Dalt. Trans., 2013, 42, 701–708.
57 B. Liu, A. Rose, N. Zhang, Y. Y. Hu and M. Ma, J. Phys. Chem. C, 2017, 121, 12610–12616.
58 M. Bishop, N. Shahid, J. Yang and A. R. Barron, Dalt. Trans., 2004, 2621–2634.
59 M. Touboul and E. Bétourné, Solid State Ionics, 1996, 84, 189–197.
60 K. Karuppasamy, J. Theerthagiri, D. Vikraman, C.J. Yim, S. Hussain, R. Sharma, T. Maiyalagan, J. Qin and H.S. Kim, Polymers (Basel)., 2020, 12, 918.
61 R. Ratti, Adv. Chem., 2014, 2014, 1–16.
62 Z. Lei, B. Chen, Y. M. Koo and D. R. MacFarlane, Chem. Rev., 2017, 117, 6633–6635.
63 M. Kar, O. Tutusaus, D. R. MacFarlane and R. Mohtadi, Energy Environ. Sci., 2019, 12, 566–571.
64 I. Popov, R. L. Sacci, N. C. Sanders, R. A. Matsumoto, M. W. Thompson, N. C. Osti, T. Kobayashi, M. Tyagi, E. Mamontov, M. Pruski, P. T. Cummings and A. P. Sokolov, J. Phys. Chem. C, 2020, 124, 8457–8466.
65 V. A. Azov, K. S. Egorova, M. M. Seitkalieva, A. S. Kashin and V. P. Ananikov, Chem. Soc. Rev., 2018, 47, 1250–1284.
66 B. R. S. Hansen, M. Paskevicius, M. Jørgensen and T. R. Jensen, Chem. Mater., 2017, 29, 3423–3430.
67 Y. Bai, X. Wang, X. Zhang, H. Shu, X. Yang, B. Hu, Q. Wei, H. Wu and Y. Song, Electrochim. Acta, 2013, 109, 355–364.
68 C. Song, W. Wang, H. Peng, Y. Wang, C. Zhao, H. Zhang, Q. Tang, J. Lv, X. Du and Y. Dou, Appl. Sci., 2018, 8, 378.
69 M. Joos, C. Schneider, A. Münchinger, I. Moudrakovski, R. Usiskin, J. Maier and B. V. Lotsch, J. Mater. Chem. A, 2021, 9, 16532–16544.
70 A. Gradišek, M. Jørgensen, M. Paskevicius, B. R. S. Hansen and T. R. Jensen, J. Phys. Chem. C, 2021, 125, 5534–5541.
71 A. V. Skripov, R. V. Skoryunov, A. V. Soloninin, O. A. Babanova, V. Stavila and T. J. Udovic, J. Phys. Chem. C, 2018, 122, 3256–3262.
72 A. Gradišek, M. Krnel, M. Paskevicius, B. R. S. Hansen, T. R. Jensen and J. Dolinšek, J. Phys. Chem. C, 2018, 122, 17073–17079.

73 R. Asakura, L. Duchêne, R. S. Kühnel, A. Remhof, H. Hagemann and C. Battaglia, ACS Appl. Energy Mater., 2019, 2, 6924–6930.
74 S. Payandeh, R. Asakura, P. Avramidou, D. Rentsch, Ł. Zbigniew, C. Radovan, A. Remhof and C. Battaglia, Chem. Mater., 2020, 32, 1101–1110.
75 F. Han, Y. Zhu, X. He, Y. Mo and C. Wang, Adv. Energy Mater., 2016, 6, 1501590.
76 M. J. Wang, R. Choudhury and J. Sakamoto, Joule, 2019, 3, 2165–2178.
77 J. Sakamoto, Nat. Energy, 2019, 4, 827–828.
78 Y. Lu, C.Z. Zhao, H. Yuan, X.B. Cheng, J.Q. Huang and Q. Zhang, Adv. Funct. Mater., 2021, 31, 2009925.
79 E. Kazyak, R. Garcia-Mendez, W. S. LePage, A. Sharafi, A. L. Davis, A. J. Sanchez, K. H. Chen, C. Haslam, J. Sakamoto and N. P. Dasgupta, Matter, 2020, 2, 1025–1048.
80 J. Su, X. Huang, Z. Song, T. Xiu, M. E. Badding, J. Jin and Z. Wen, Ceram. Int., 2019, 45, 14991–14996.
81 S. Kim, K. Harada, N. Toyama, H. Oguchi, K. Kisu and S. Orimo, J. Energy Chem., 2020, 43, 47–51.
82 L. Cheng, E. J. Crumlin, W. Chen, R. Qiao, H. Hou, S. Franz Lux, V. Zorba, R. Russo, R. Kostecki, Z. Liu, K. Persson, W. Yang, J. Cabana, T. Richardson, G. Chen and M. Doeff, Phys. Chem. Chem. Phys., 2014, 16, 18294–18300.
83 M. S. Whittingham, Science (80-.)., 1976, 192, 1126–1127.
84 J. Xie and Y.C. Lu, Nat. Commun., 2020, 11, 2499.
85 J. Y. Kim, J. Park, S. H. Kang, S. Jung, D. O. Shin, M. J. Lee, J. Oh, K. M. Kim, J. Zausch, Y.G. Lee and Y. M. Lee, Energy Storage Mater., 2021, 41, 289–296.
86 T. Krauskopf, H. Hartmann, W. G. Zeier and J. Janek, ACS Appl. Mater. Interfaces, 2019, 11, 14463–14477.
87 C. Lu, C. Dong, H. Wu, D. Ni, W. Sun, Z. Wang and K. Sun, Chem. Commun., 2018, 54, 3235–3238.